Supporting Information

Spectroelectrochemistry with Hydrogen-Doped Indium Oxide Electrodes Monitors Electron and Hole Injection into PbS Quantum Dots

Sophia Westendorf, Shangjing Li, Patrick Michel, Bin Hu, and Marcus Scheele

EMAS Measurements of Blank IHO Substrates

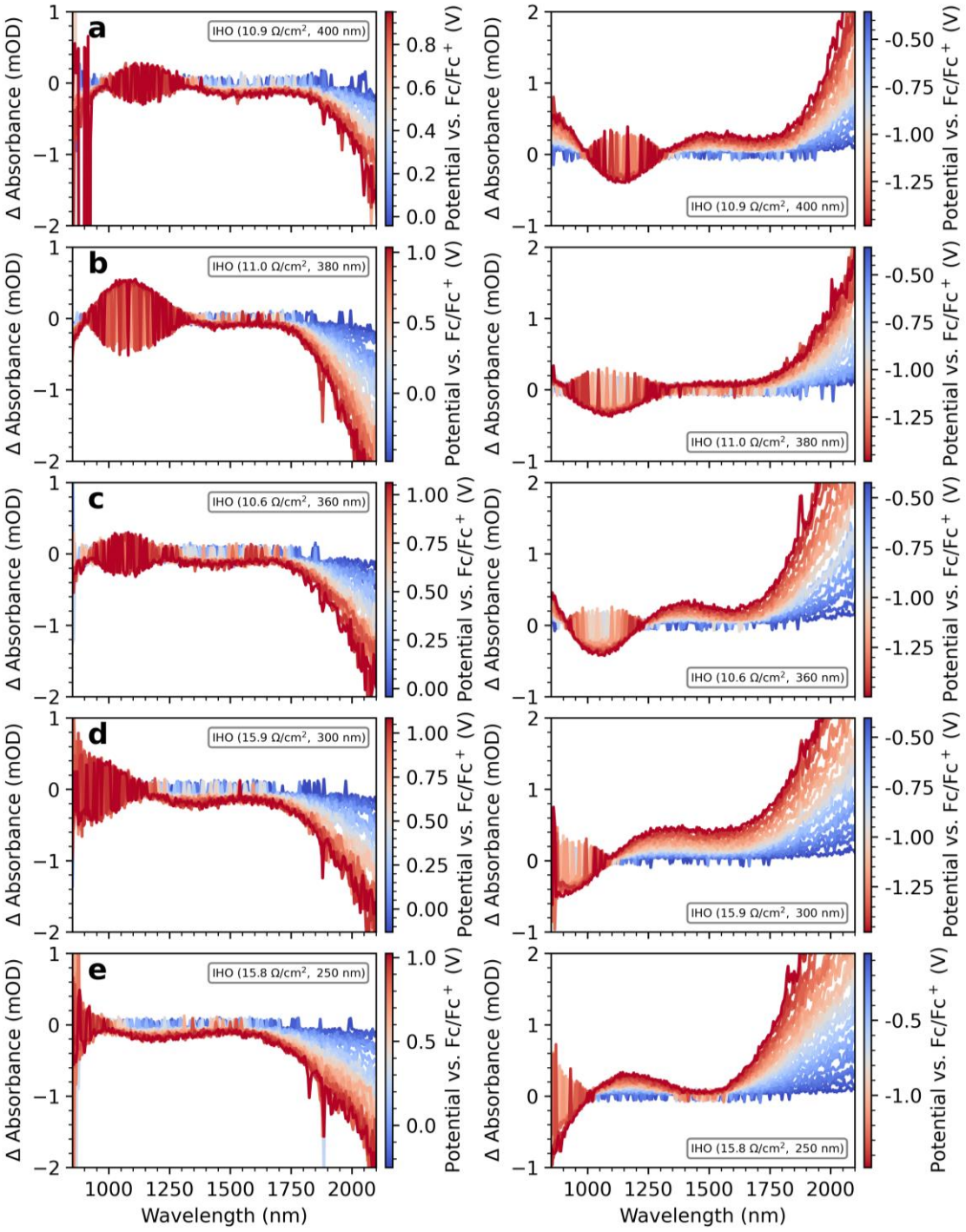

Figure S1: Oxidative (left panel) and reductive (right panel) EMAS Spectra of uncoated IHO substrates of different preparation parameters. The measurements were conducted in $LiClO_4$/MeCN-d_3 starting at the respective OCP. Applied potentials vs. Fc/Fc^+ are indicated by the colour code.

Table S1: Overview of spectroscopic and spectroelectrochemical features observed during absorption and reductive EMAS measurements.

# IHO	Film Thickness [nm]	Sheet Resistance [Ω/sq]	Sputter Time [min]	Absorption Peak [nm]	EMAS Bleach [nm]	Zero-Crossing [nm]	Crossing $\Delta A > 5*10^{-4}$ [nm]
1-1	400	10.9	30	985	1150	1330	1870
1-2	400	10.9	30	985	1150	1320	1800
3-1	360	10.6	35	915	1050	1250	1750
7-2	300	15.9	25	785	900	1100	1650
8-2	380	11.0	30	930	1100	1340	1860
9-1	380	10.8	30	935	1090	1270	1790
11-2	380	10.8	30	905	1050	1250	1700
12-1	250	15.8	20	660	N/A	1020	1690

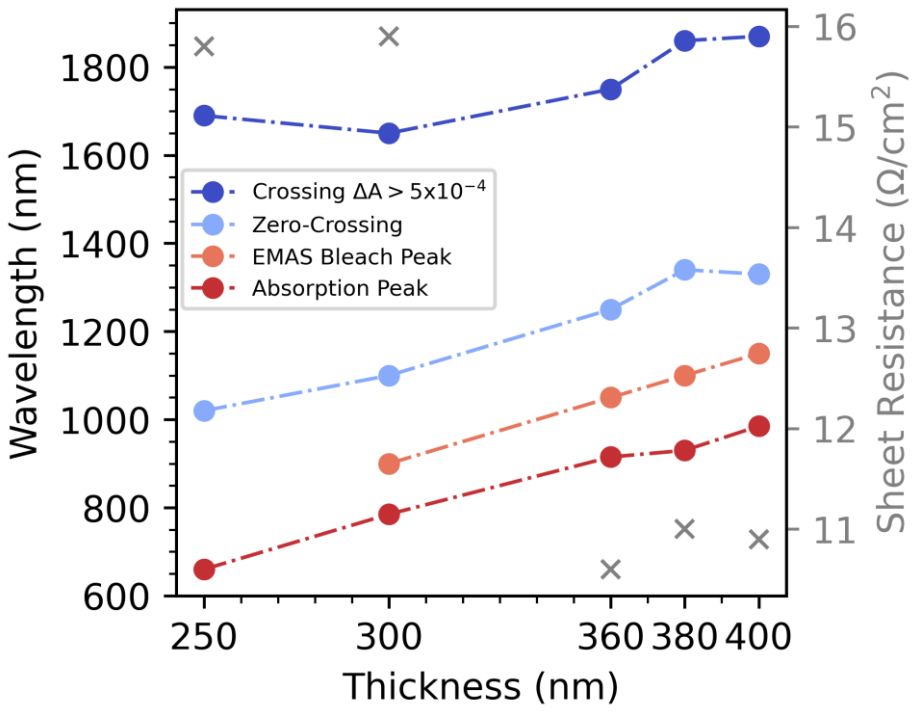

Figure S2: Comparison of the IHO film thickness and resulting spectroscopic and spectroelectrochemical features.

EMAS Blank IHO in TBAHFP/MeCN-d_3

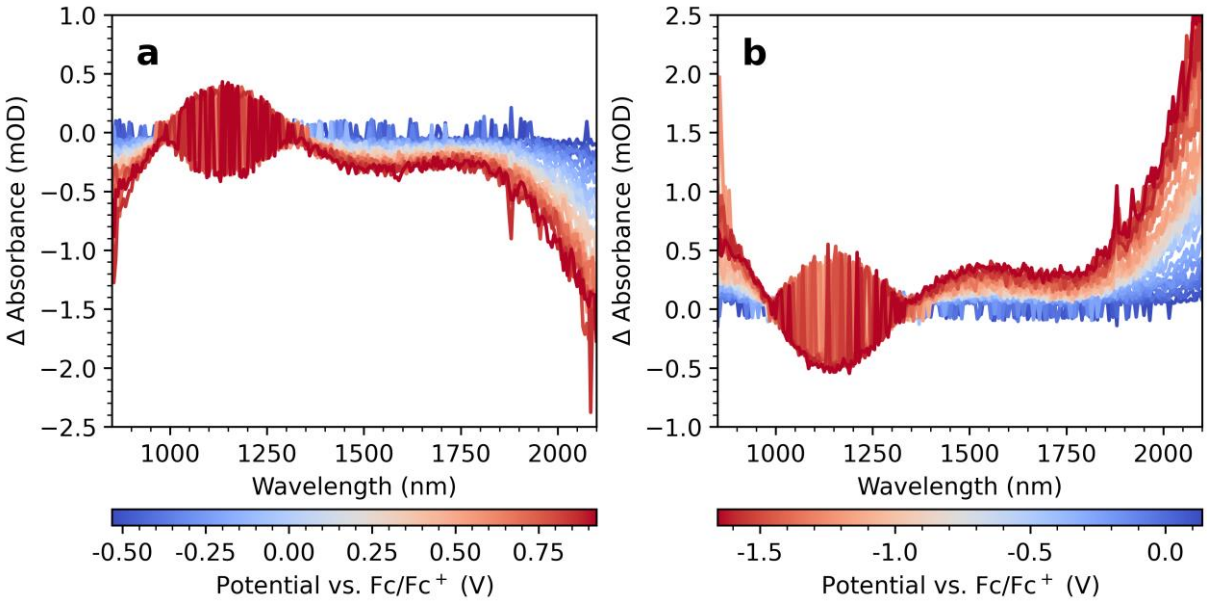

Figure S3: Oxidative (a) and reductive (b) EMAS measurements of blank IHO substrates measured in TBAHFP/MeCN-d_3.

EMAS of FTO Substrates

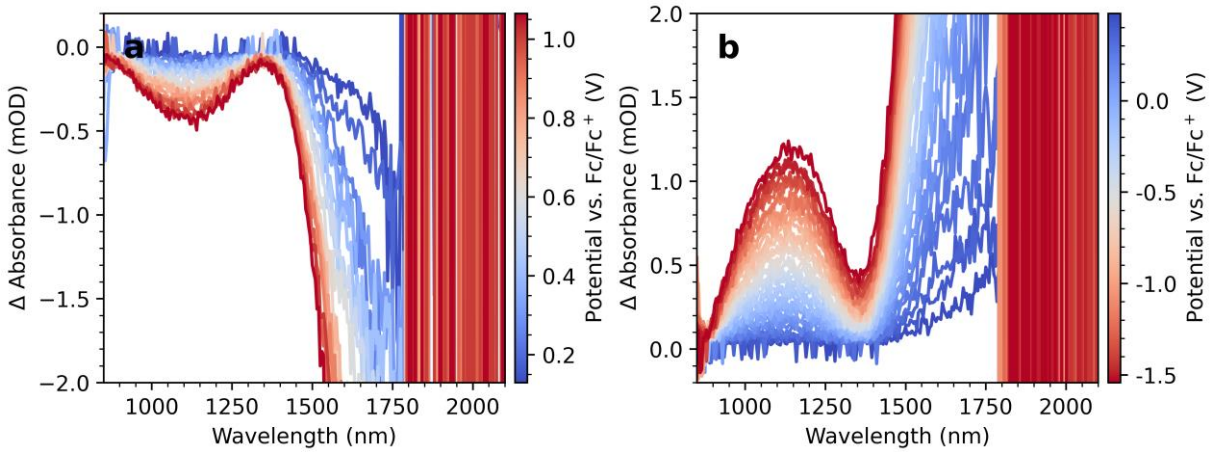

Figure S4: Oxidative (a) and reductive (b) EMAS measurement of an uncoated FTO (7 Ω/sq) with $LiClO_4$/MeCN-d_3 as electrolyte solution. Reduction of the material leads to an induced absorption between 880 nm and 1350 nm with a peak at 1150 nm. At wavelengths above 1400 nm, the absorbance change increases drastically. A mirrored image is observed upon oxidation, with a slight bleach between 880 nm and 1350 nm, peaking at 1140 nm and an extreme decrease in absorbance change at wavelengths above 1400 nm. The onset potentials for both scan directions are in the vicinity of the respective OCP and the intensity increases when going to more extreme potentials. At wavelengths above 1800 nm only noise is measured.

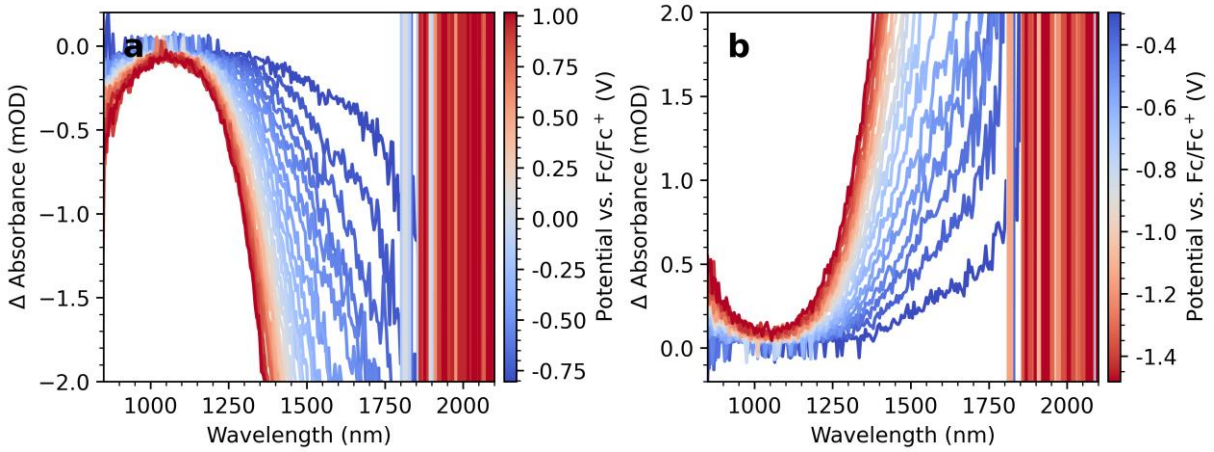

Figure S5: Oxidative (a) and reductive (b) EMAS measurement of an uncoated FTO (15 Ω/sq) with $LiClO_4$/MeCN-d_3 as electrolyte solution. During both measurements, in a spectral range of 900 to 1200 nm, almost no absorbance change is observed. Above 1200 nm a large increase (decrease) in absorbance change is recorded for reductive (oxidative) EMAS measurements.

CV Measurements of PbS QDs

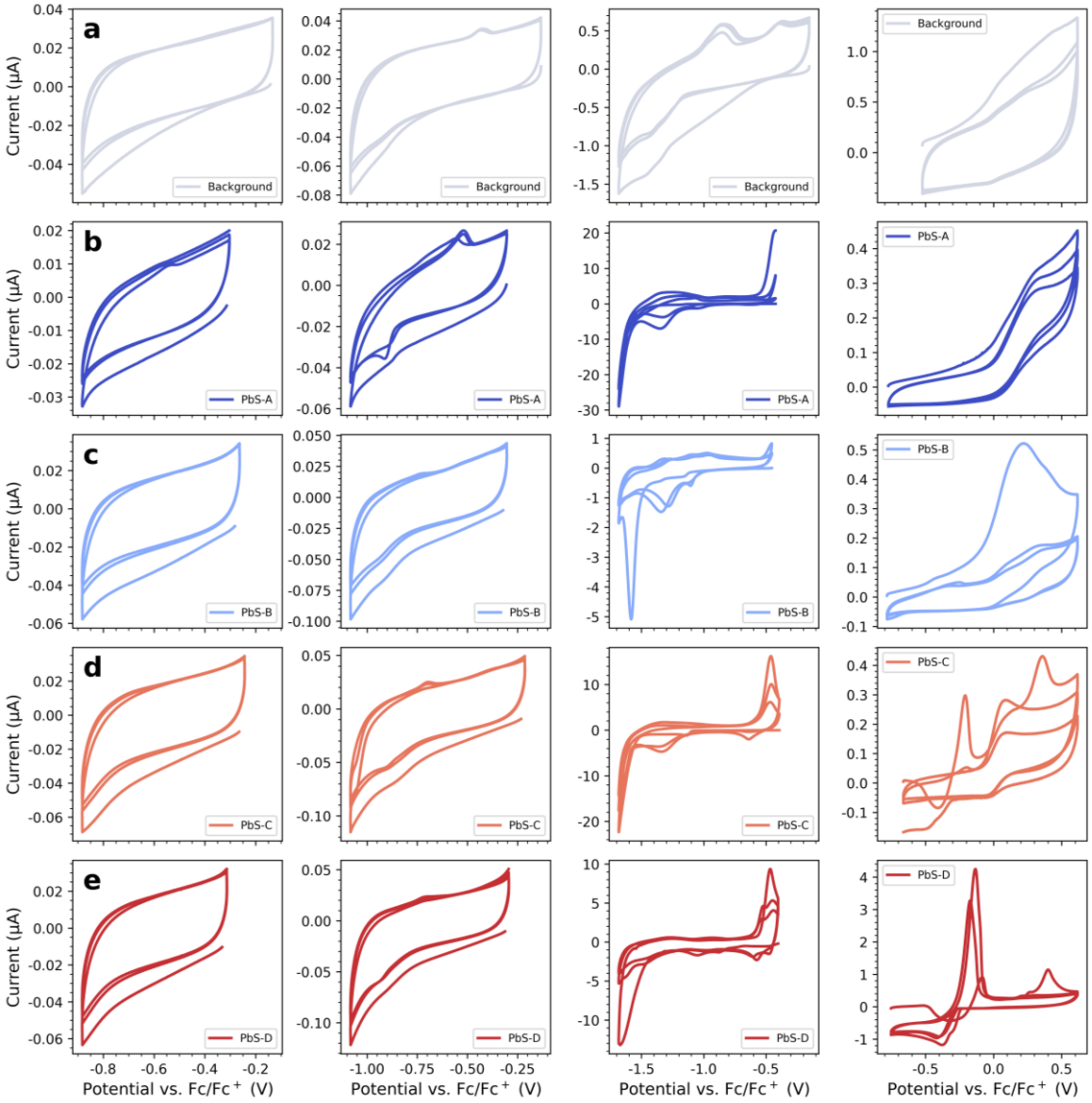

Figure S6: CV Measurements of a) Clean GC Electrode, b) PbS-A, c) PbS-B, d) PbS-C, and e) PbS-D in 0.1 M TBAHFP/MeCN measured from the respective OCP to -0.8 V, -1.0 V, -1.6 V and 0.7 V vs. Fc/Fc^+ (column-wise from left to right).

Effect of MeCN-d_3

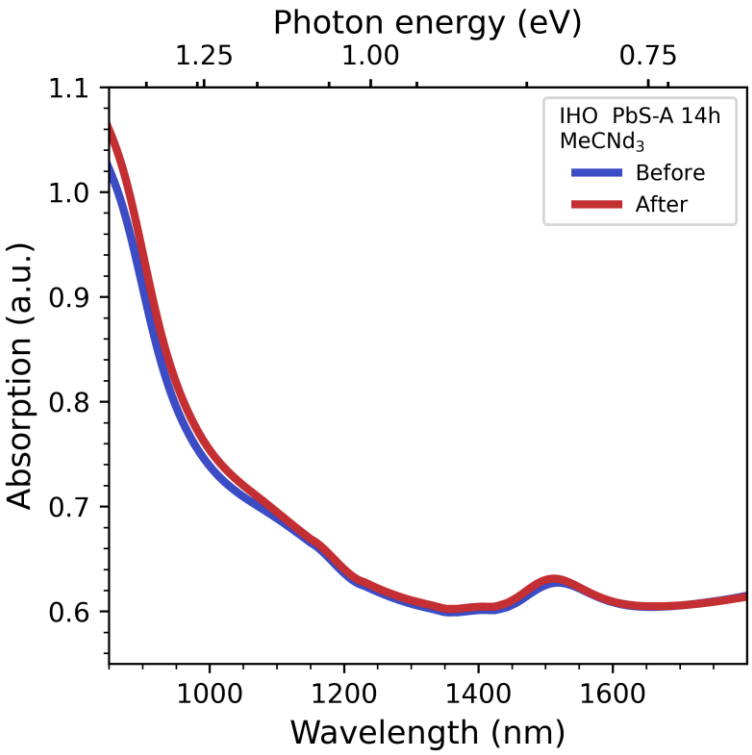

Figure S7: PbS-A film on IHO before and after 14h in MeCN-d_3.

Second oxidative and reductive EMAS Measurements

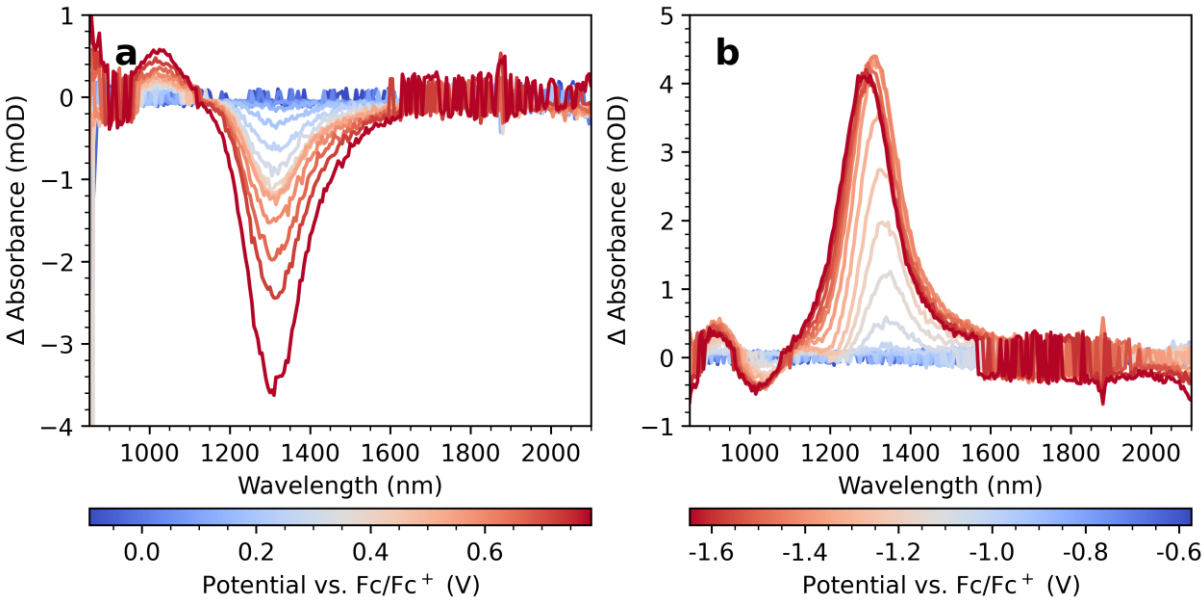

Figure S8: Second oxidative (a) and reductive (b) EMAS measurements of PbS-A in TBAHFP/MeCN-d_3. The measurements followed the scans shown in **Figure 4a** and **Figure 4c** respectively and were started at newly determined OCPs.

EMAS Measurements of PbS-B, PbS-C and PbS-D

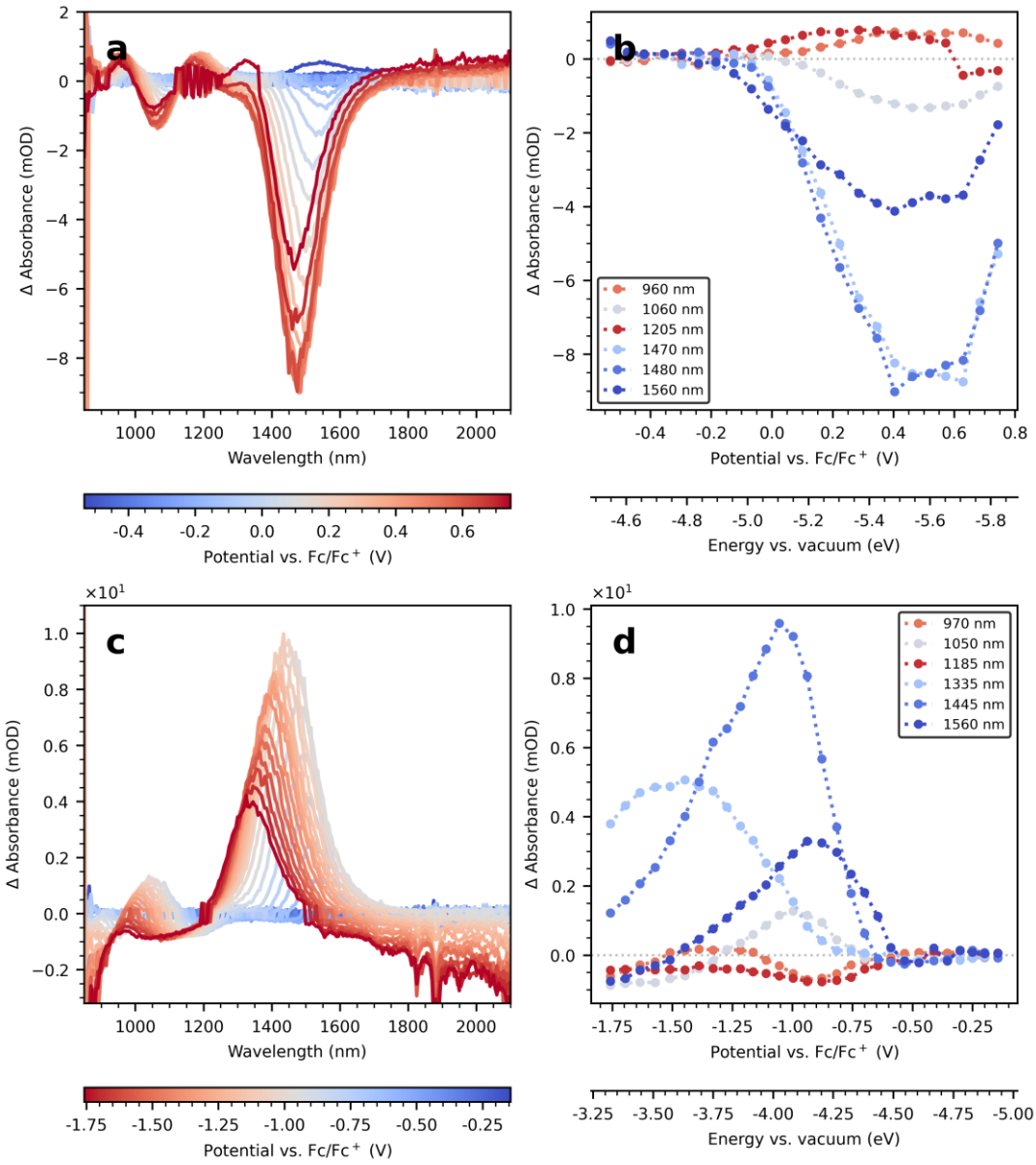

Figure S9: Oxidative (a) and reductive (c) EMAS measurement of PbS-B on IHO as working electrode and linecuts (b, d) at specific wavelengths.

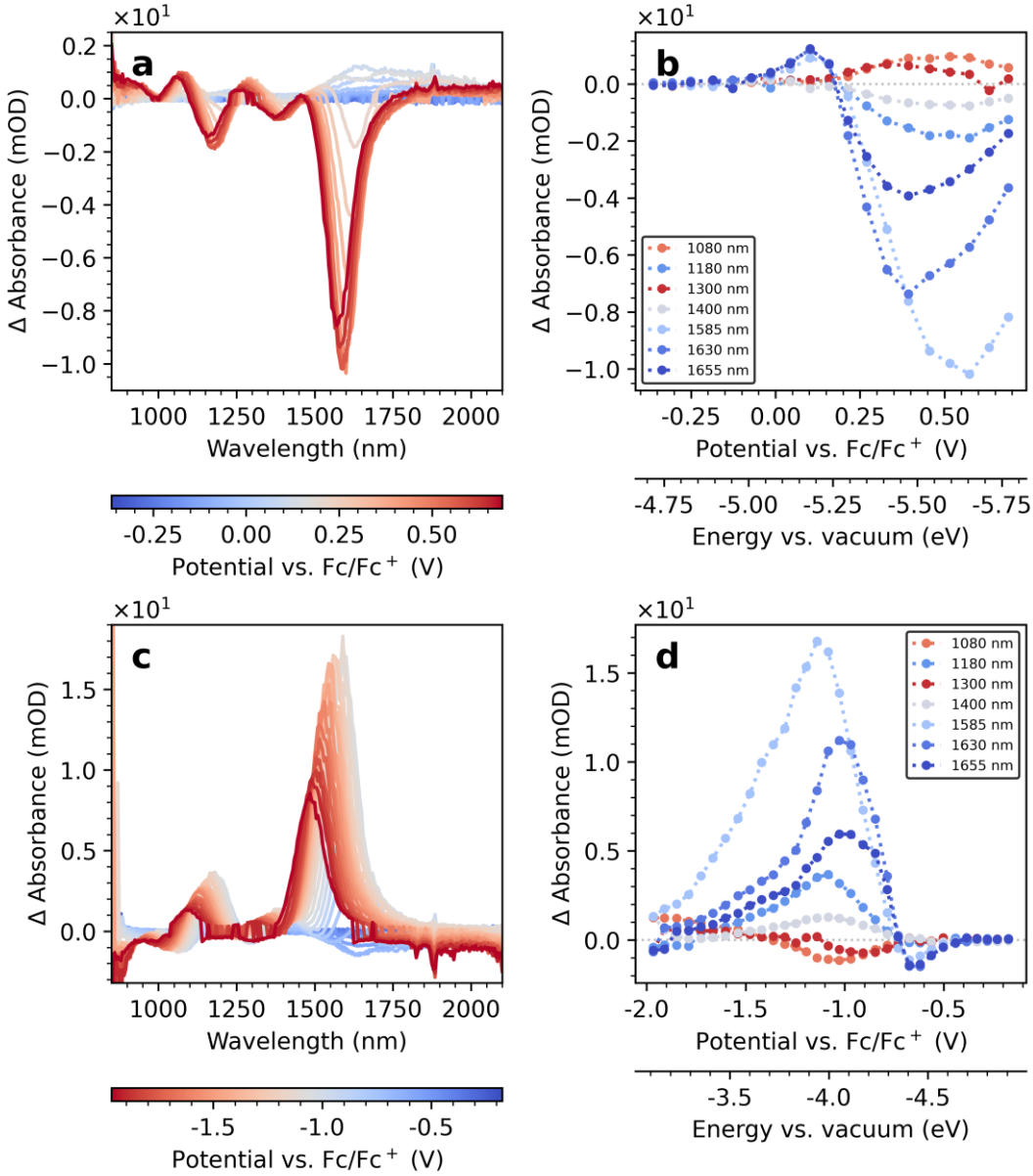

Figure S10: Oxidative (a) and reductive (c) EMAS measurement of PbS-C on IHO as working electrode and linecuts (b, d) at specific wavelengths.

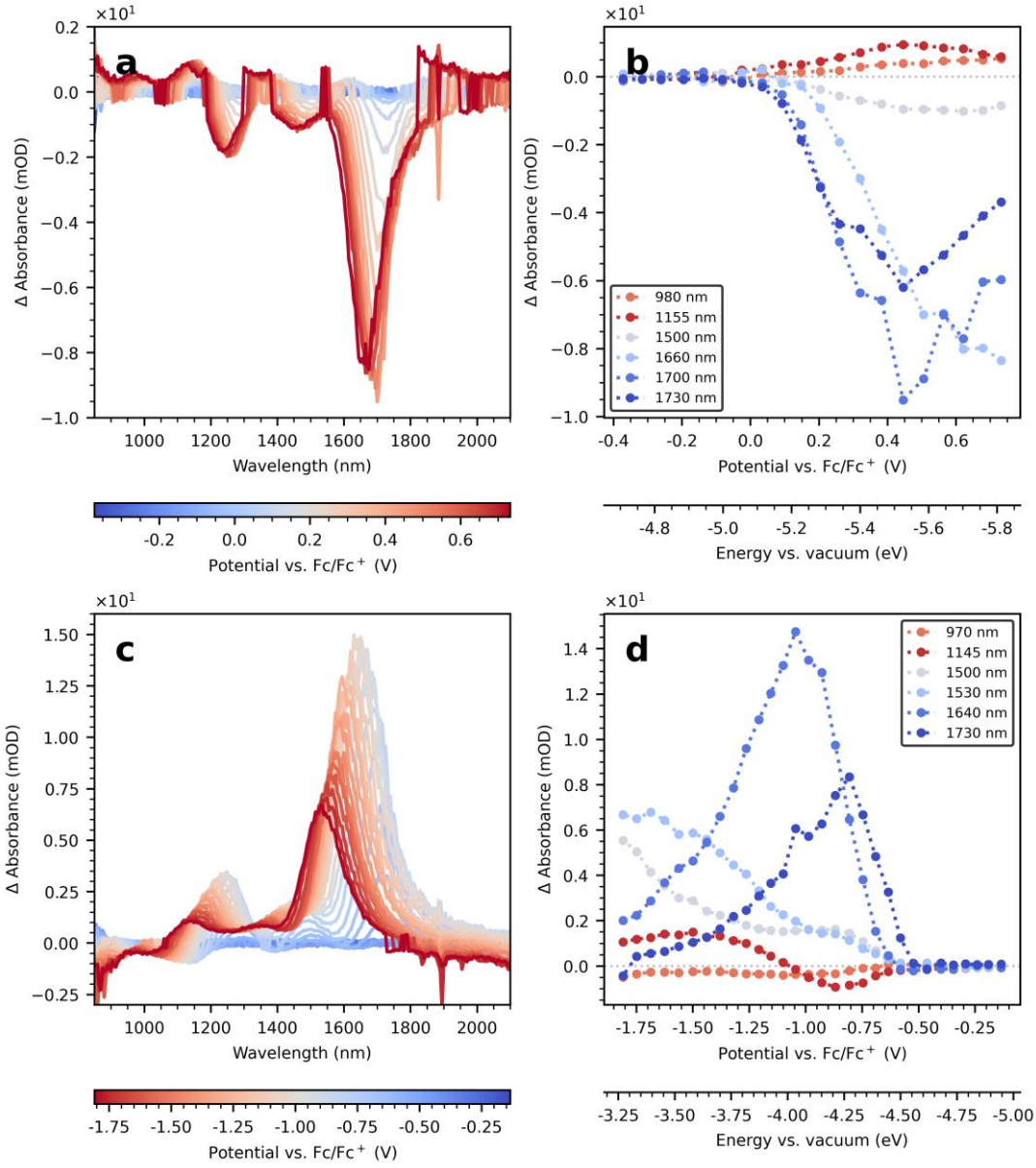

Figure S11: Oxidative (a) and reductive (c) EMAS measurement of PbS-D on IHO as working electrode and linecuts (b, d) at specific wavelengths.

Comparison of PbS EMAS Spectra

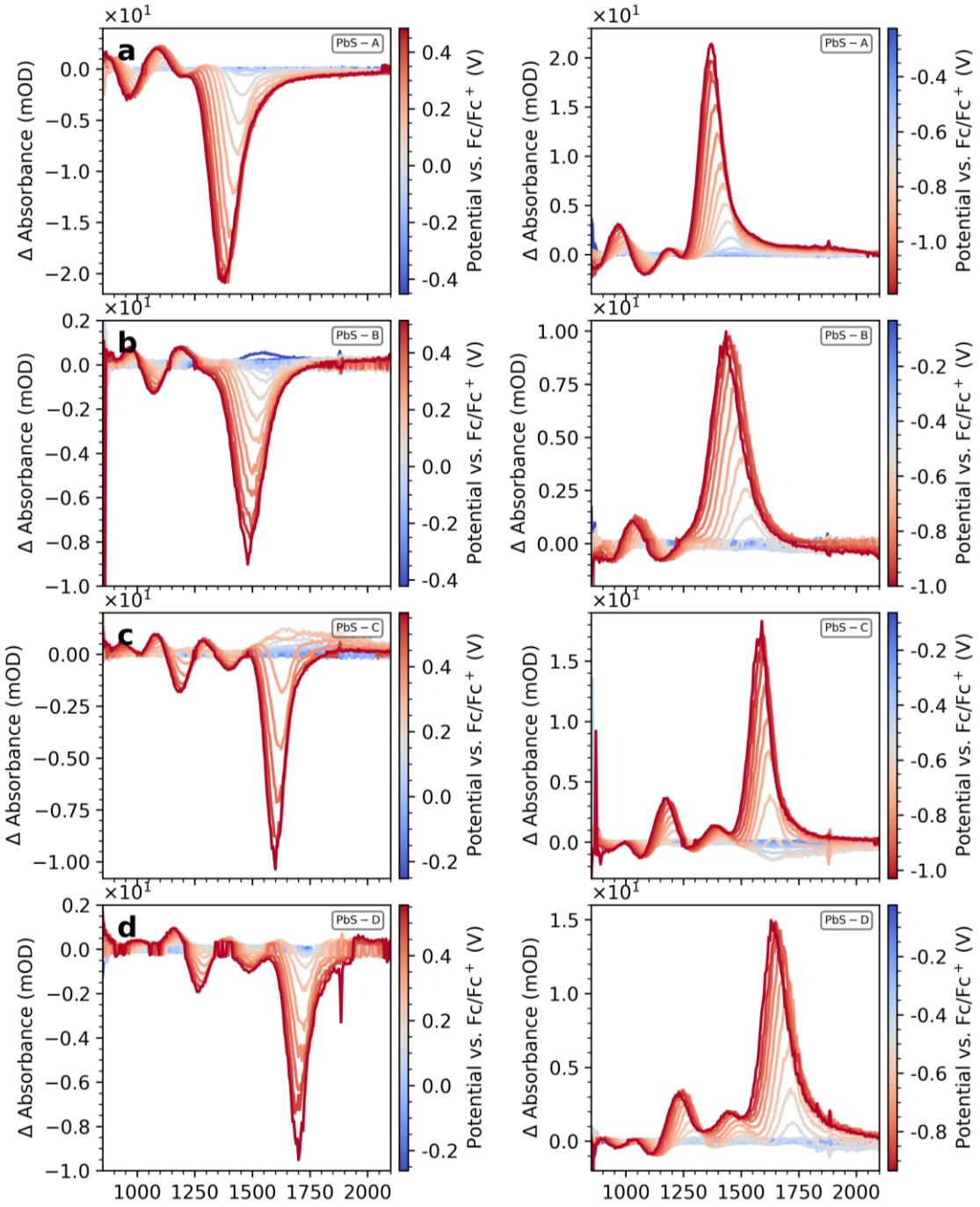

Figure S12: EMAS spectra plotted up to peak potentials for a) PbS-A, b) PbS-B, c) PbS-C, and d) PbS-D.

EMAS PbS-A in $LiClO_4$/MeCN-d_3

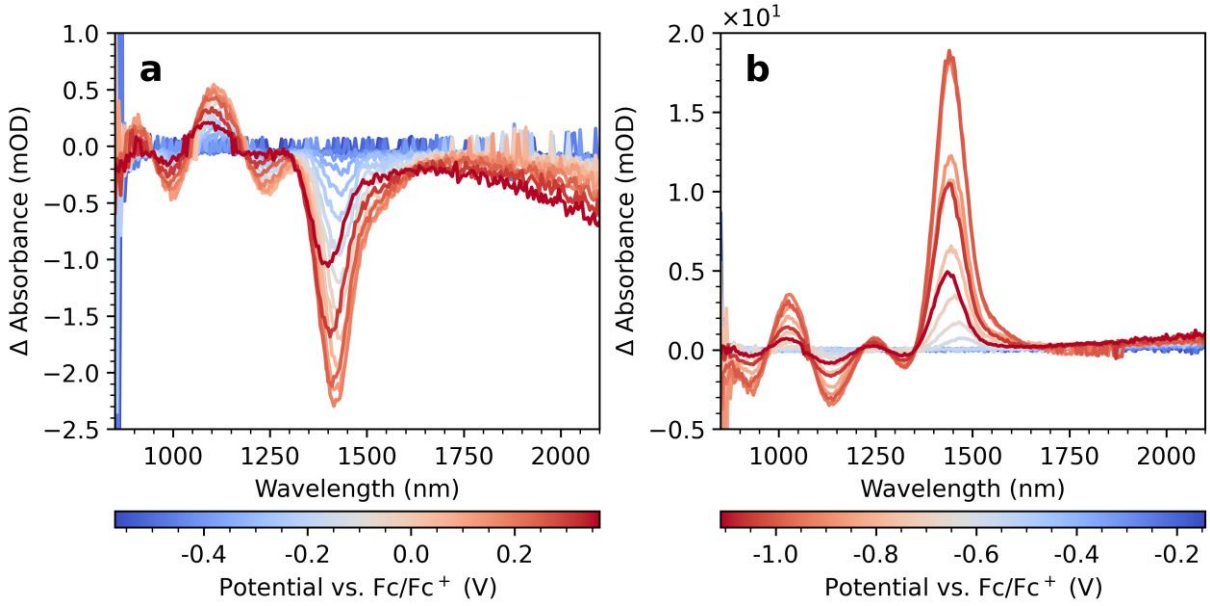

Figure S13: Oxidative (a) and reductive (b) EMAS measurements of PbS-A in $LiClO_4$/MeCN-d_3.

EMAS Measurements in a Reduced Wavelength Range

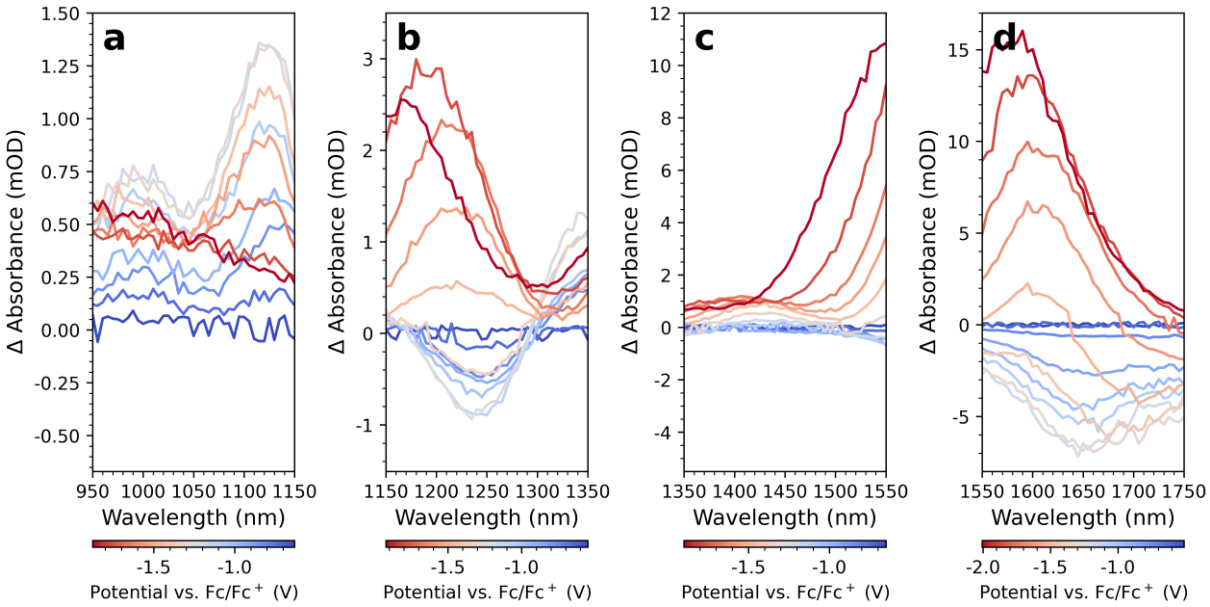

Figure S14: Small range EMAS measurements of PbS-C.

EMAS Phase Relation

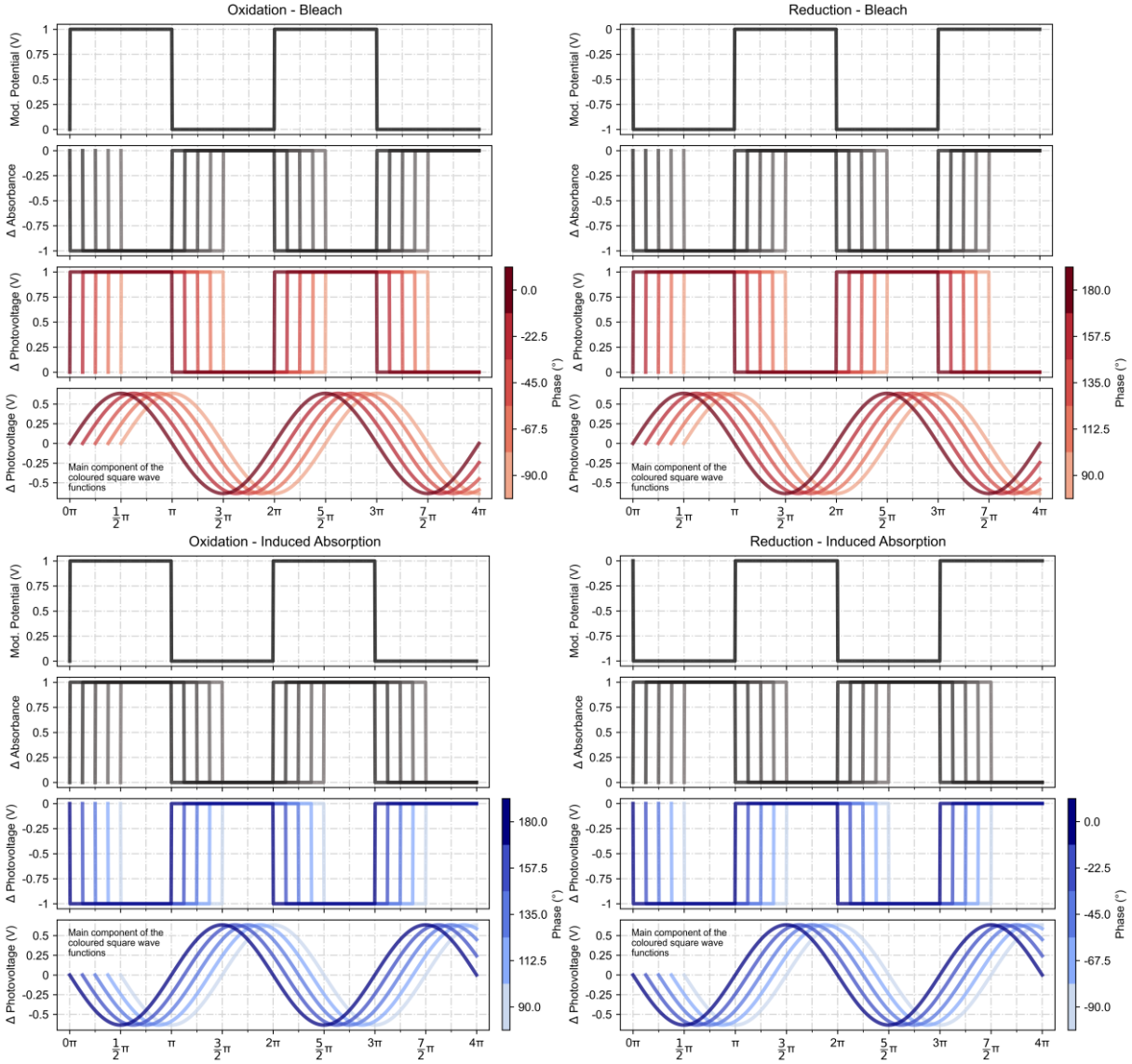

Figure S15: Phase relation between the square-wave modulated potential and the potential-dependent absorption change.

Phase Development of PbS EMAS Measurements

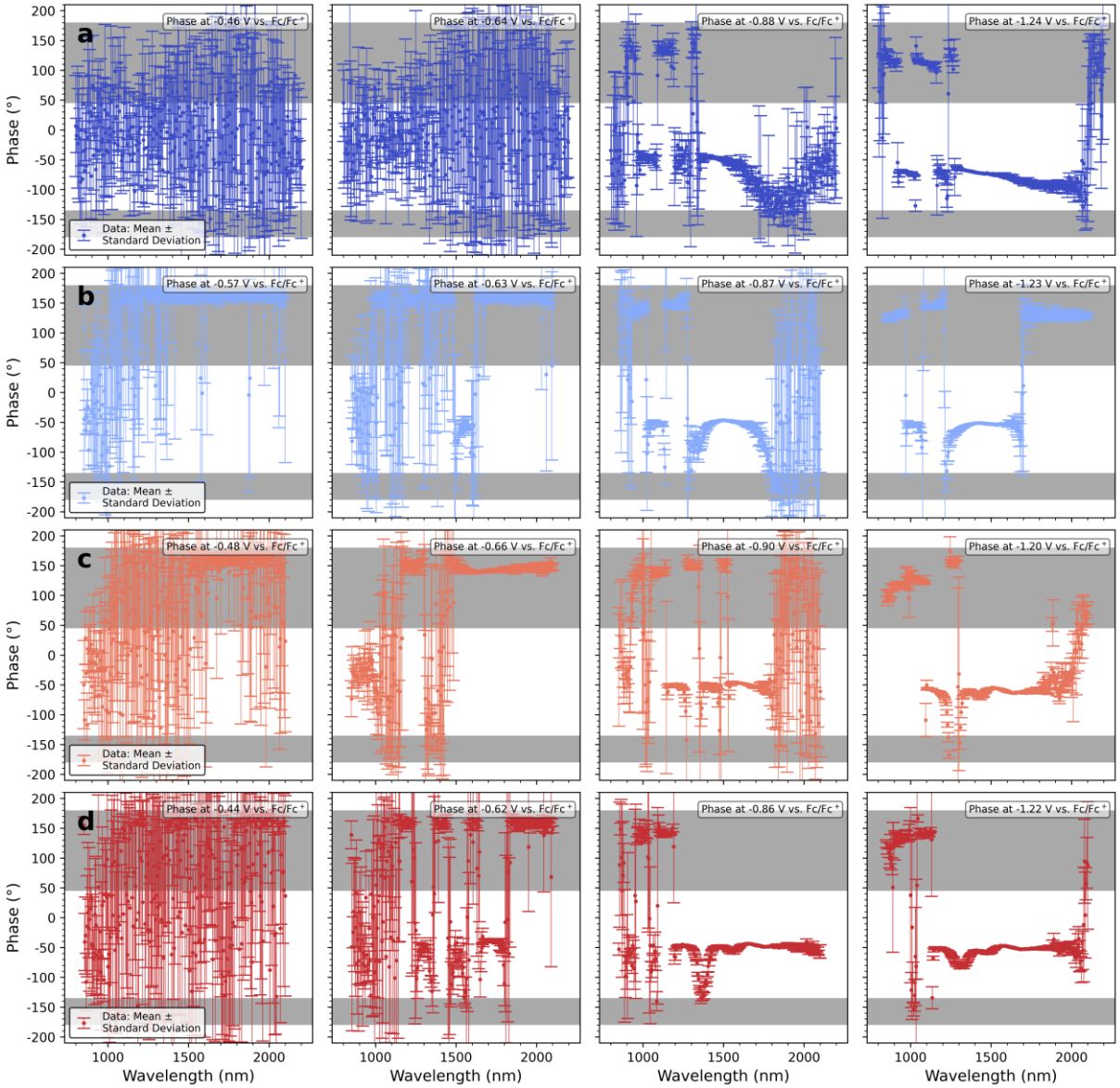

Figure S16: Phase development of a) PbS-A, b) PbS-B, c) PbS-C, and d) PbS-D during reductive EMAS measurements. Grey coloured areas mark phase ranges which are considered as a bleach.

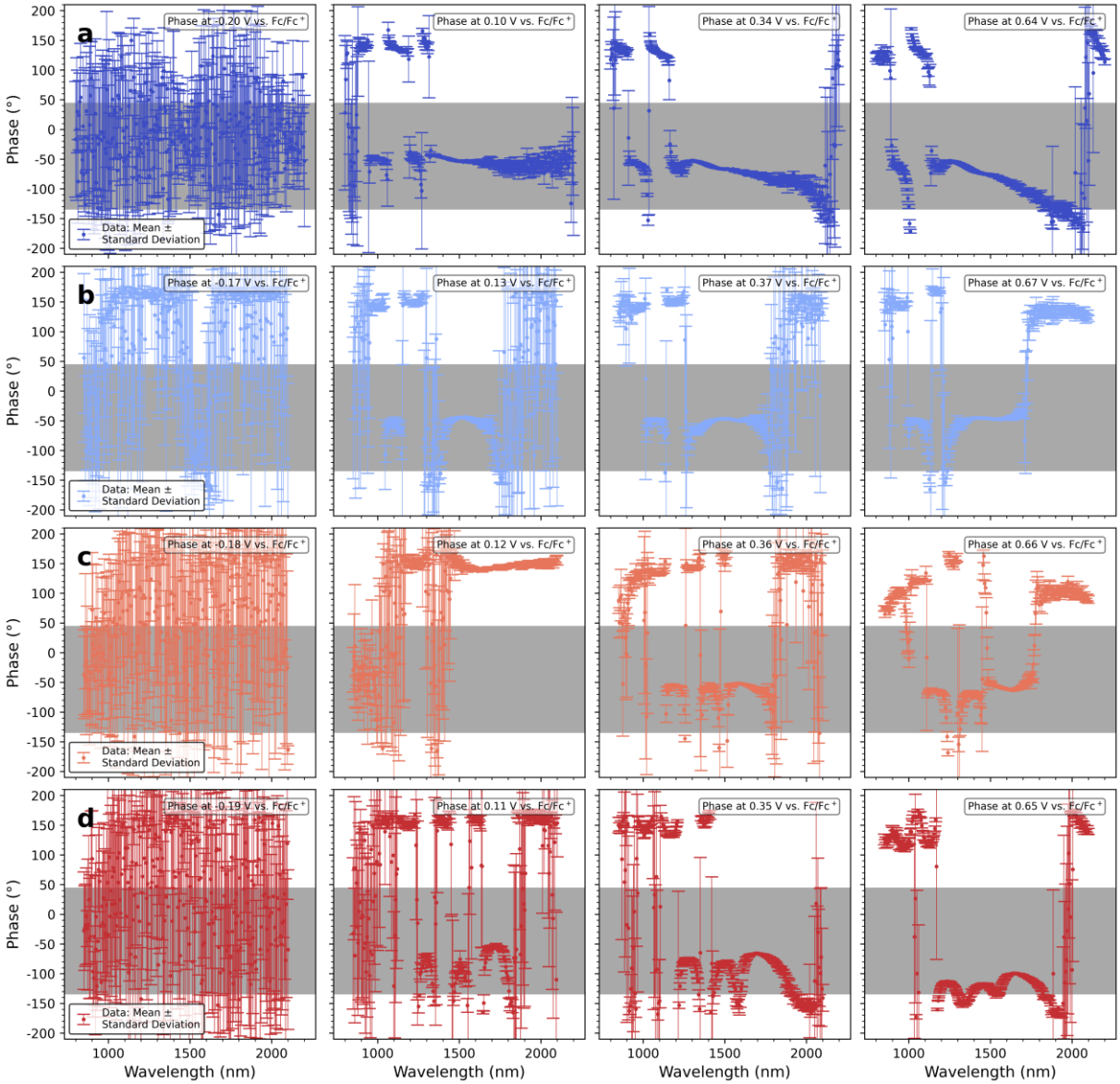

Figure S17: Phase development of a) PbS-A, b) PbS-B, c) PbS-C, and d) PbS-D during oxidative EMAS measurements. Grey coloured areas mark phase ranges which are considered as a bleach.

CV Measurements of Ferrocene

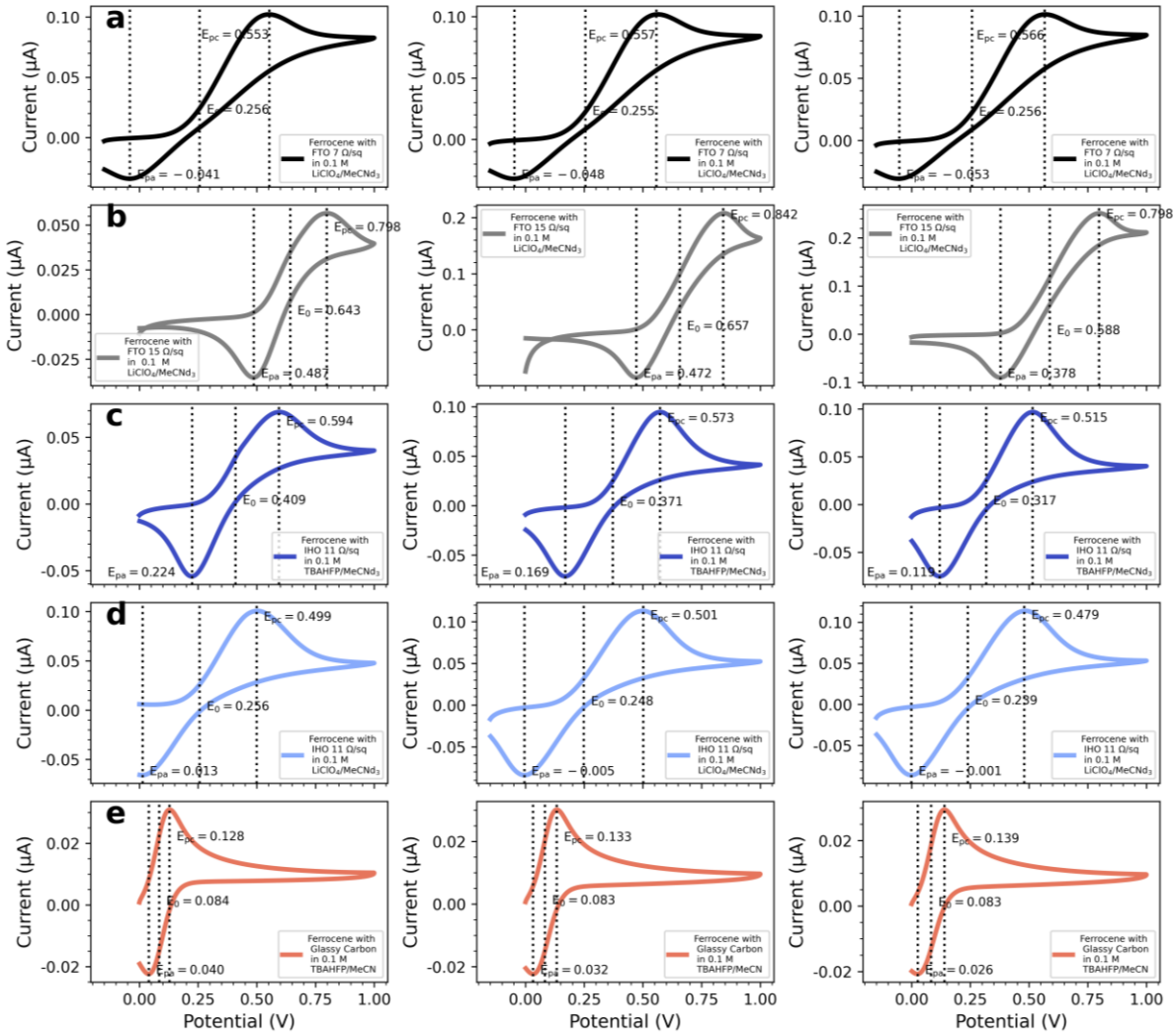

Figure S18: CV Measurements of Ferrocene with a) FTO 7 Ω/sq in $LiClO_4$/MeCN-d_3 ($\varnothing E_0$ = 0.256 V), b) FTO 15 Ω/sq in $LiClO_4$/MeCN-d_3 ($\varnothing E_0$ = 0.629 V), c) IHO 11 Ω/sq in TBAHFP/MeCN-d_3 ($\varnothing E_0$ = 0.357 V), d) IHO 11 Ω/sq in $LiClO_4$/MeCN-d_3 ($\varnothing E_0$ = 0.247 V), e) GC Electrode in TBAHFP/MeCN ($\varnothing E_0$ = 0.083 V).

EMAS Setup

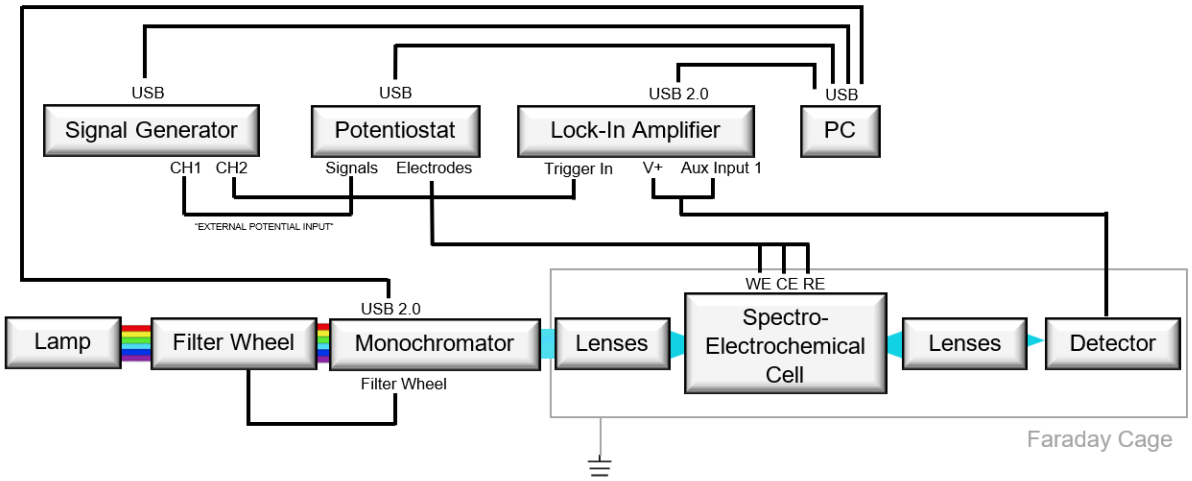

Figure S19: Schematic representation of the EMAS setup with its components, its connections and the beam path.

SEM Images and Size Distributions of the PbS QDs

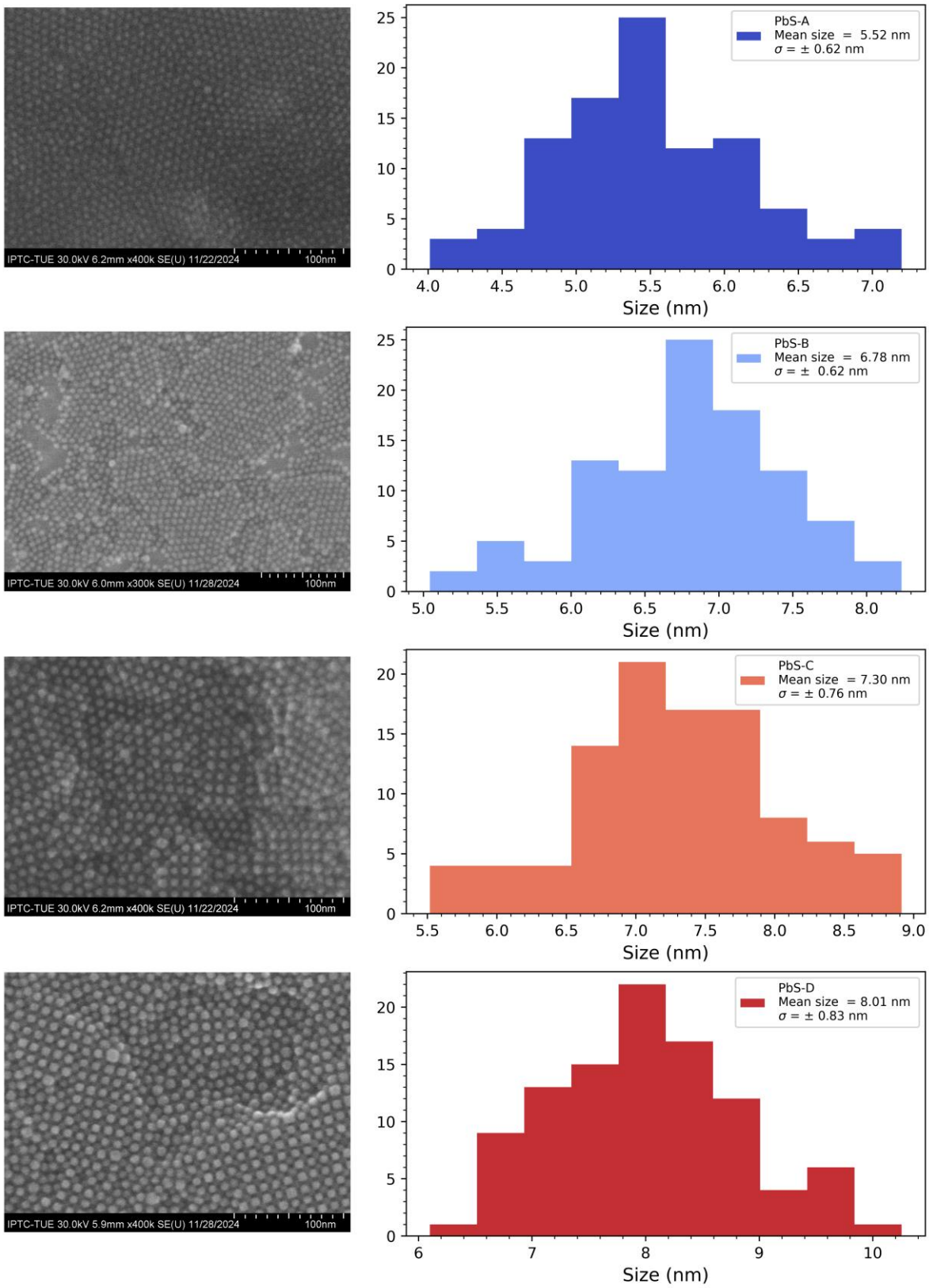

Figure S20: SEM images (left panel) and determined size distributions (right panel) of the PbS QDs.

Profilometer

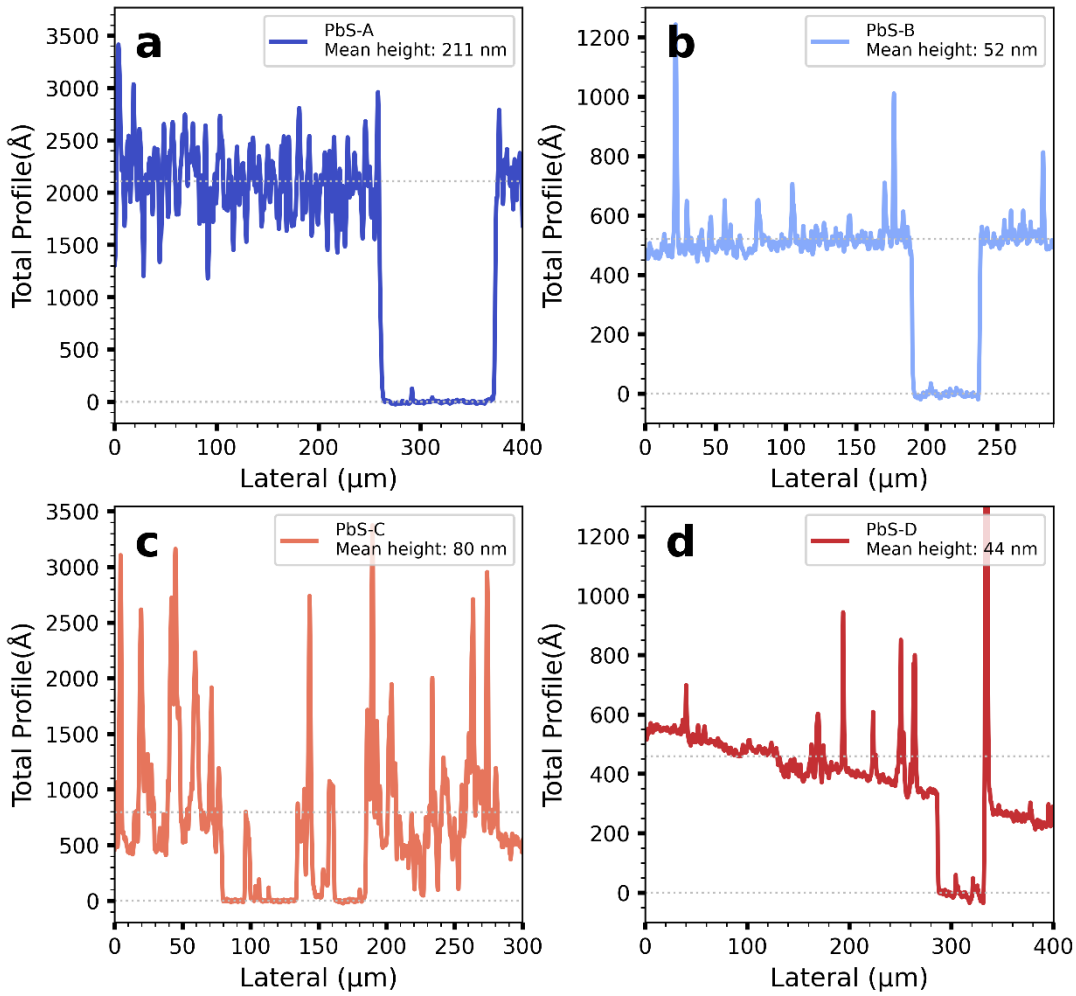

Figure S21: Profilometer measurements of the PbS film thickness of the EMAS samples.

Characterisation of IHO Substrates

To examine the robustness of the preparation method, the absorbance and transmittance of two pieces cut from the same IHO coated glass slide are shown in **Figure S22a**. At wavelengths below 1200 nm, the samples show the same spectral properties and at higher wavelengths, the differences are negligibly small. Additionally, the reproducibility of the preparation process was verified by comparing two IHO substrates from different batches with the same preparation parameters (sputter time etc.), resulting in the same film thicknesses and sheet resistances, are compared in **Figure S22b**. While the overall shape of the two spectra is alike, there is a slight shift visible, which is due to slightly different thicknesses resulting from varying sputtering times.

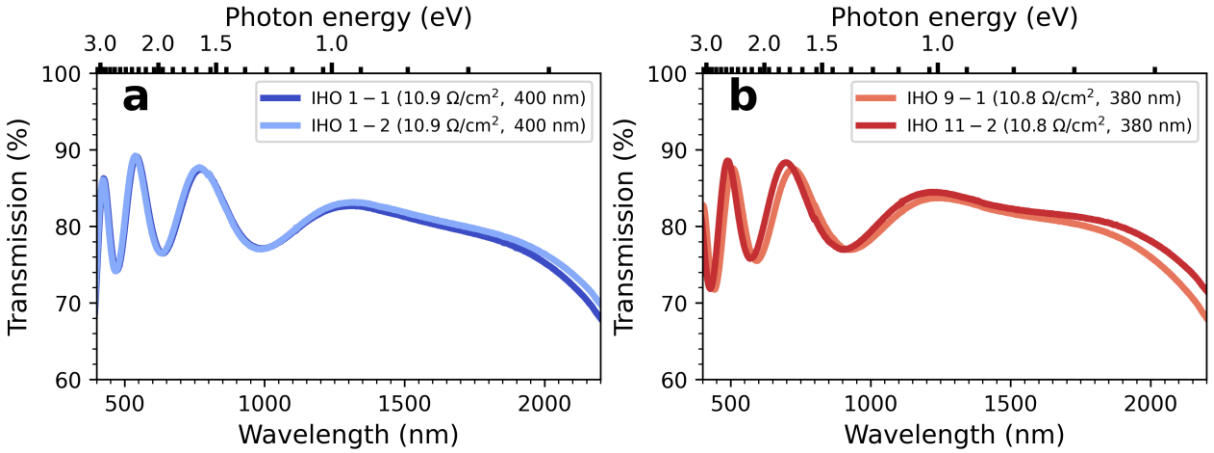

Figure S22: a) Visible and NIR transmittance spectra of two IHO substrates of the same preparation batch. b) Visible and NIR transmittance spectra of two IHO substrates of the same sheet resistance (10.8 Ω/sq) and film thickness stemming from different preparation batches.

The surface properties of the IHO film were investigated using ultraviolet photoelectron spectroscopy (UPS) and X-ray photoelectron spectroscopy (XPS). For each characterization, the annealed IHO sample was immediately transferred to the test chamber.

For UPS, prior to the test, the sample surface was sputtered with Ar ions （2 keV，2 μA）for 20 s to remove surface contamination, and a clean Au foil was used as a reference for energy calibration based on the Au $4f_{7/2}$ transition at 84.0 eV. A -5 V bias voltage was applied during the measurement of the secondary electron cutoffs.

From the UPS spectra (**Figure S23**), the work function of the IHO sample was determined to be 3.7 eV, and the valence band maximum (VBM) is at a binding energy (BE) of 3.03 eV.

The XPS spectra of H_2-doped In_2O_3 (IHO) and undoped In_2O_3 samples, both prepared using the same method except for the substitution of the sputtering gas with pure Ar in the undoped sample, are shown in **Figure S24**. The In $3d_{5/2}$ peaks, located around ~444 eV, are primarily attributed to the indium oxide species. Notably, the undoped film exhibited a slightly higher binding energy, approximately 0.4 eV, compared to the IHO film, which is closer to the binding energy of indium hydroxide species (~445.1 eV). This suggests the likely presence of hydrogen dopants in the film and their influence on the chemical state of indium. Generally, the lower binding energy observed in the IHO film correlates with an increased electron density, consistent with the widely accepted understanding that hydrogen acts as a shallow donor in IHO, facilitating an increase in electron density.

Significant differences were observed in the O 1s XPS spectrum of the two samples. In **Figure S24b**, the IHO sample shows two distinct peaks at ~529.6 eV and ~532.2 eV, which are attributed to lattice oxygen species and oxygen vacancy species, respectively. Therefore, hydrogen doping is believed to facilitate the crystallization of the IHO film and suppress oxygen vacancies, which benefits electron transfer and enhances the mobility of IHO. However, this aspect is not the primary focus of this study and we will not go into further detail.

The XRD pattern of an IHO substrate is shown in **Figure 25** with "PDF #06-0416" used as a standard XRD card for In_2O_3 film from the JCPDS database.

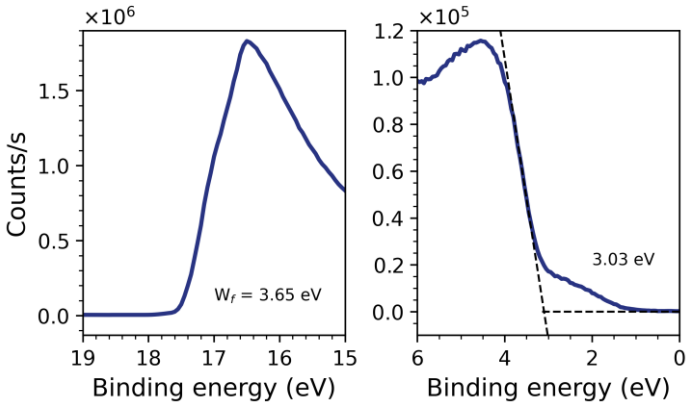

Figure S23: UPS spectra of the prepared IHO film.

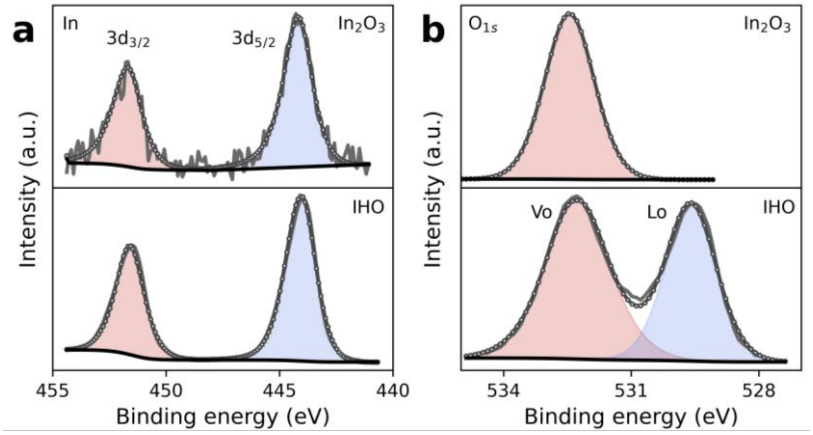

Figure S24: XPS spectrum of undoped In_2O_3 and IHO film. (a) In 3d; (b) O_{1s}.

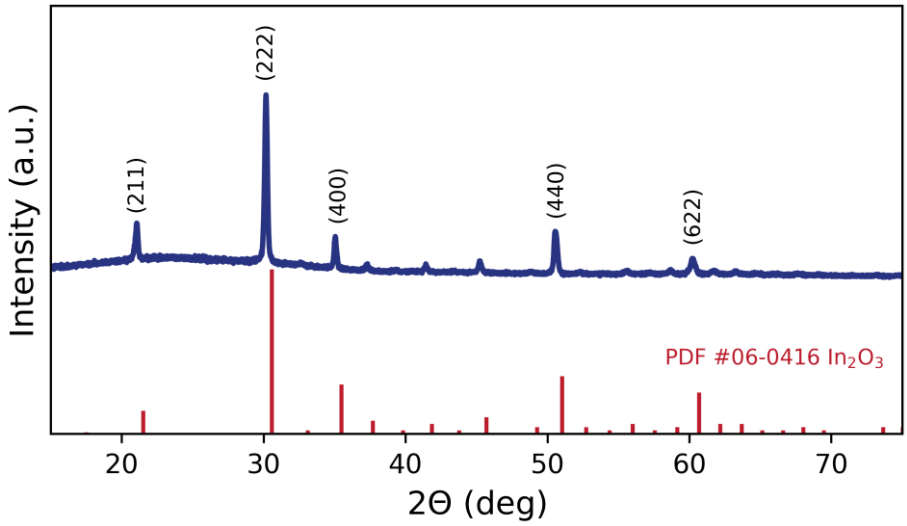

Figure S25: XRD pattern of the IHO film.